

# Image of Fomalhaut Dust Ring at 350 $\mu\text{m}$ : Relative Column Density Map Shows Pericenter-Apocenter Asymmetry

K. A. Marsh<sup>1,2</sup>, T. Velusamy<sup>1,3</sup>, C. D. Dowell<sup>1,4</sup>, K. Grogan<sup>1,5</sup>, and C. A. Beichman,<sup>6</sup>

## ABSTRACT

We have imaged the circumstellar disk of Fomalhaut at 350  $\mu\text{m}$  wavelength, using SHARC II at the Caltech Submillimeter Observatory. The spatial resolution of the raw images ( $9''$ ) has been enhanced by a factor of three using the HiRes deconvolution procedure. We find that at this wavelength and signal to noise ratio ( $\sim 12$ ), the observed morphology is that of a simple inclined ring ( $i \simeq 70^\circ$ ), with little or no other apparent structure—this is the first observation that shows clearly the ring morphology of the disk. We have combined our 350  $\mu\text{m}$  data with *Spitzer Space Telescope* images at 24, 70, and 160  $\mu\text{m}$  in order to estimate the 2-dimensional spatial variation of relative column density (“tau map”) using our DISKFIT procedure. The tau map is based on the following physical assumptions: (1) the wavelength variation of opacity is the same throughout the disk, (2) the radial variation of dust temperature is dictated by the energy balance of individual grains in the stellar radiation field, and (3) the vertical scale height of the disk follows a power-law radial variation. The results confirm the ring-like morphology, but also show that the geometric center is displaced from the star by about 8 AU and that the ring has an apocentric enhancement of approximately 14% in integrated column density. If we interpret the displacement in terms of elliptical orbital motion due to gravitational perturbation by an unseen planet, then the implied forced eccentricity is  $\sim 0.06$ ; dynamical modeling then predicts an apocentric density enhancement consistent with that inferred from the tau map.

---

<sup>1</sup>Jet Propulsion Laboratory, 4800 Oak Grove Drive, Pasadena, CA 91109

<sup>2</sup>E-mail: Kenneth.A.Marsh@jpl.nasa.gov

<sup>3</sup>E-mail: Thangasamy.Velusamy@jpl.nasa.gov

<sup>4</sup>E-mail: cdd@submm.caltech.edu

<sup>5</sup>E-mail: Keith.Grogan@jpl.nasa.gov

<sup>6</sup>California Institute of Technology 100-22, Pasadena, CA 91125; E-mail: chas@ipac.caltech.edu

*Subject headings:* circumstellar matter — planetary systems — stars: individual (Fomalhaut)

## 1. Introduction

The study of dusty debris disks around main sequence stars can provide clues to the possible presence of orbiting bodies such as planets, the gravitational effects of which have predictable effects on the orbital dynamics of dust particles (see, for example, Quillen & Thorndike (2002); Wilner et al. (2002)). One system of considerable interest is Fomalhaut ( $\alpha$  PsA), of which submillimeter-wave mapping at 450 and 850  $\mu\text{m}$  has shown the presence of structure dominated by a pair of intensity maxima interpreted as the ansae of an inclined ring (Holland et al. 2003). Observations at 24, 70, and 160  $\mu\text{m}$  with *Spitzer* (Werner et al. 2004) show that the relative intensities of the ansae are wavelength-dependent (Stapelfeldt et al. 2004).

The spatial variation of dust column density in the disks provides information about the perturbing bodies when interpreted using dynamical models. However, since the observed (intensity) images are sensitive to variations in dust temperature as well as column density, we clearly need a tool to separate these effects. With this in mind, we have developed an inversion procedure (DISKFIT) designed to estimate the 2-dimensional spatial distribution of optical depth (or relative column density) of a circumstellar disk in either the sky plane or disk plane, given a set of observed images at multiple wavelengths, the corresponding point source response functions (PSFs), and certain model assumptions. We have applied this procedure to our new 350  $\mu\text{m}$  image of Fomalhaut in conjunction with *Spitzer* data.

## 2. Observations and Data Reduction

Fomalhaut was observed at 350  $\mu\text{m}$  with the SHARC II camera (Dowell et al. 2003) at the Nasmyth focus of the Caltech Submillimeter Observatory (CSO) on 2004 Sep 18 UT. Of a total period of 4.7 hr on source, three hour-long integrations between 8.5 and 12.3 h UT provided the best signal-to-noise due to low atmospheric opacity (0.039 at 225 GHz, 1.05 at 350  $\mu\text{m}$ ; both at zenith), remarkable atmospheric stability, and relatively high source elevation ( $27^\circ$  to  $41^\circ$ ). Our final map therefore consists of a coaddition of the images from that period, with a total integration time of 3.0 hr.

The telescope executed a Lissajous scanning pattern with peak-to-peak amplitude  $60''$  and period 20 s in the azimuth direction, and peak-to-peak amplitude  $30''$  and period 14.14 s in the elevation direction. Of the 12 rows of the detector array, only rows 1–8 were operational for this run; at a plate scale of  $4''.57 \text{ pixel}^{-1}$ , the instantaneous field of view was then  $146'' \times 37''$ . The bolometer signals were sampled at 28 Hz and then reduced with the CRUSH software program (A. Kovacs, in preparation <sup>1</sup>). We used the “-deep” option which takes a more aggressive approach at modeling atmospheric and instrumental effects, but found the results to be relatively insensitive to this choice, perhaps due to the atmospheric stability. Automatic correction was made for the atmospheric opacity and increased gain of the detectors under reduced atmospheric loading, the latter being a  $\sim 6\%$  effect implemented using a lookup table.

Absolute calibration was accomplished with hourly, interspersed observations of Uranus and Neptune. Uranus (assumed flux  $237 \text{ Jy beam}^{-1}$ , 250 Jy total) was observed at elevations of  $59^\circ$  and  $31^\circ$ , and Neptune (assumed flux  $92 \text{ Jy beam}^{-1}$ , 94 Jy total) was observed at elevations of  $42^\circ$  and  $29^\circ$ . The resultant four scale factors from instrument units to Jy  $\text{beam}^{-1}$  had a relative RMS of 7%. We estimate an absolute flux calibration accuracy of 20% and pointing accuracy of  $2''$ . The PSF (FWHM  $\simeq 9''$ ) was obtained from observations of Neptune, appropriately rotated and coadded so as to recreate accurately the rotational smearing due to the changing parallactic angle during the Fomalhaut observations.

The upper panel of Figure 1 shows the resulting image of Fomalhaut at  $350 \mu\text{m}$ . The integrated flux density is  $1.18 \pm 0.24 \text{ Jy}$ . In order to enhance the spatial resolution of the image, we have deconvolved it using the HiRes implementation (Backus et al. 2005) of the Maximum Correlation Method (Aumann, Fowler & Melnyk 1990). The result is shown in the lower panel of Figure 1, the spatial resolution of which is approximately  $3''$ . It is apparent that the source is strikingly symmetrical, suggestive of a simple ring. This is, in fact, the first observation which clearly shows the ring-like morphology. A key question, though, is whether the dust ring is truly uniform or has density variations. We have addressed this issue by combining our  $350 \mu\text{m}$  image with other data using our DISKFIT inversion procedure.

### 3. Estimation of Relative Column Density Distribution

The principal model assumptions involved in DISKFIT are:

1. The wavelength variation of opacity,  $\kappa(\lambda)$ , is the same throughout the disk; we have

---

<sup>1</sup>see <http://www.submm.caltech.edu/~sharc/crush/index.htm>

assumed a power-law variation of the form  $\kappa(\lambda) \propto \lambda^{-\beta}$ .

2. The radial variation of dust temperature is given by the energy balance of individual grains (Backman & Paresce 1993), based on a grain size-scale parameter,  $\lambda_0$ , which represents the wavelength above which the grains radiate inefficiently.
3. The vertical scale height of the disk follows a power-law variation with respect to radial distance,  $r$ . In terms of the opening angle,  $\psi$ , corresponding to 1 scale height above and below midplane, we have assumed  $\psi(r) = \psi_{100}(r_{\text{[AU]}}/100)^\gamma$ , where  $\psi_{100}$  is the opening angle at  $r = 100$  AU.

There are two main steps in the inversion procedure:

**Step 1: Parameter Estimation.** In this initial step, we obtain estimates of some preliminary parameters necessary for the optical depth mapping. These parameters consist of  $\beta$ ,  $\psi_{100}$ , and  $\gamma$  (defined above), the disk inclination,  $i$ , with respect to the sky plane, and the position angle,  $\theta$ , of the tilt axis. We base these estimates on a simple model involving a circular disk of inner and outer radii  $r_{\text{in}}$  and  $r_{\text{out}}$ , respectively, with a power-law radial dependence of optical depth (normal to disk plane), represented by  $\tau(r) \propto r^{-\alpha}$ . Allowance is made for the possibility that the center of the dust ring may be displaced from the star, as an approximate way of taking into account the effects of orbital ellipticity. A maximum likelihood estimate is then made of the full set of parameters characterizing this model, using the set of observed images and PSFs, taking account of the measurement noise in each observed image, and making allowance for the presence of small errors in the position calibration of each observed image.

**Step 2: Inversion for Optical Depth Map.** Based on the estimated values of  $i$ ,  $\theta$ ,  $\psi_{100}$ ,  $\gamma$ , and  $\beta$  from the previous step, the full inversion for the 2-dimensional distribution of line-of-sight optical depth (referred to as a “tau map”) in the plane of the sky is accomplished using an algorithm which is similar mathematically to the Richardson-Lucy procedure (Richardson 1972; Lucy 1974). Since the PSFs at each wavelength are implicitly deconvolved using the prior knowledge of positivity of optical depth, some superresolution is obtained. The output is a map of the line-of-sight optical depth at an arbitrary reference wavelength (equivalent to relative column density) and the associated uncertainty map. As a final step, we can transform this sky projection into a pole-on view using a linear estimation procedure which takes into account the flared geometry.

### 3.1. Application to Fomalhaut

The input data for the parameter-fit step consisted of our 350  $\mu\text{m}$  image and *Spitzer* images at 160 and 70  $\mu\text{m}$  from the Multiband Imaging Photometer for *Spitzer* (MIPS)—see Rieke et al. (2004). Although a MIPS image at 24  $\mu\text{m}$  was also available, we did not include it in this step since it contains a significant response to the presence of an additional warm dust component (Stapelfeldt et al. 2004) which was not included in the simple ring model. Both large (blackbody) and intermediate-sized ( $\lambda_0 = 27 \mu\text{m}$ ; Backman & Paresce (1993)) grains were considered for the purpose of the dust temperature calculation. Although the results were not strongly dependent on the assumed grain properties, the best fit was obtained under the blackbody assumption, consistent with the presence of large grains as inferred by Chini et al. (1990).

The complete set of estimated parameter values is given in Table 1, with error bars representing the effect of random measurement noise;  $\Delta x$  and  $\Delta y$  represent the estimated offsets of the center of the dust ring with respect to the star, in a right-handed coordinate system in which the  $y$ -axis corresponds to the disk tilt axis (positive = NNW). We have verified that the results are unaffected by the possible effects of imperfect removal of an instrumental near-IR leak in the 160  $\mu\text{m}$  image by repeating the fit excluding the 160  $\mu\text{m}$  data; there was no significant difference in the estimated parameters.

Figure 2 shows the residual images from the uniform-ring model fit as compared to the observed images; each plot represents a slice along the major axis of the tilted ring. The residuals are more or less consistent with the estimated background noise and correspond to a  $\chi^2_\nu = 1.56$ . The fact that the latter value is somewhat larger than unity suggests the possibility of a slight deviation from a uniform ring.

The next step (tau map estimation) involved reprocessing the raw images, making use of the above estimates of  $i$ ,  $\theta$ ,  $\psi_{100}$ ,  $\gamma$ , and  $\beta$ . The input data were the observed images at all four available wavelengths (350, 160, 70, and 24  $\mu\text{m}$ ); the resulting tau map in the sky-plane projection is shown in the left hand panel of Figure 3. In this figure, the line-of-sight optical depth variation is expressed at a reference wavelength of 24  $\mu\text{m}$ ; the spatial resolution is approximately 22 AU. The peak values of optical depth in the ring are  $(6.61 \pm 0.28) \times 10^{-3}$  and  $(6.56 \pm 0.33) \times 10^{-3}$  at the SSE and NNW ansae, respectively. The density-weighted dust temperature in the ring is 42 K. Since the uncertainty of the estimated optical depth increases with radial distance, the map has been truncated at 310 AU, at which the uncertainty is twice that at ring maximum.

It is apparent that the SSE peak on the tau map is slightly closer to the star than the NNW peak—this is consistent with the result obtained independently from the parametrized

model fit. The inferred displacement between the star and disk center results from the need to preferentially heat the SSE portion of the ring in order to reproduce the observed 30% intensity enhancement of the SSE ansa at  $70 \mu\text{m}$  (see Figure 2 and the discussion in Stapelfeldt et al. (2004)). Therefore, the estimation accuracy of the displacement ( $\pm 1$  AU) is dependent on these intensity ratios rather than the absolute pointing of the telescope. Since the tau map embodies more observational data than the model fit, we can refine our estimates of the other ring parameters; in particular we obtain 180 AU for  $r_{\text{out}}$ .

We have deprojected the tau map to produce a pole-on view of the disk, but due to the large inclination, the resulting errors were a factor of three higher than for the sky projection. The dynamic range was consequently insufficient for any further elucidation of the density structure and so we have not included the result here.

#### 4. Discussion

Our  $350 \mu\text{m}$  image is qualitatively different from the  $450 \mu\text{m}$  image published by Holland et al. (2003) in that it has the morphology of a symmetrical ring as opposed to the horseshoe shape at  $450 \mu\text{m}$  (ansae connected by a single arc). The latter was interpreted in terms of a dust “clump” suggestive of material trapped in the mean motion resonance of a large planet. Since our  $350 \mu\text{m}$  image is of similar signal to noise ratio and resolution, we should have detected such a feature (at the  $4\sigma$  level in this case). More detailed examination shows that the arclike bridge at  $450 \mu\text{m}$  has about the same relative intensity with respect to the peak (0.5) as that of either arm of the ring at  $350 \mu\text{m}$ , whereas the western arm at  $450 \mu\text{m}$  is substantially weaker ( $0.2 \times$  peak). Thus rather than the eastern arm at  $450 \mu\text{m}$  being an enhancement, the western arm is actually a depression. This argues against the presence of a dust clump in the former location.

Our estimated disk parameters agree essentially with previous values (Dent et al. 2000; Holland et al. 2003), including the opacity index ( $\beta \simeq 1$ ) which is consistent with relatively large ( $\sim 100 \mu\text{m}$ ) grains. One possible discrepancy is that our opening angle of  $17^\circ$  implies a smaller vertical disk thickness ( $\sim 40$  AU) than previous estimates ( $\sim 80$  and  $120$  AU at  $450$  and  $850 \mu\text{m}$ , respectively—Holland et al. (2003); Dent et al. (2000)). However, the estimated value is very sensitive to PSF width, suggesting that at least some of the differences may be resolution-related.

Our optical depth mapping indicated an  $\sim 8$  AU displacement of the ring center from the star. Such a displacement was suggested by Wyatt et al. (1999) as a consequence of gravitational perturbation by orbiting bodies, observable by the resulting pericenter glow;

the latter was invoked by Stapelfeldt et al. (2004) to explain the brightness asymmetry of the ansae. Our estimated displacement corresponds to a forced eccentricity of approximately 0.06, consistent with the findings of Stapelfeldt et al.

In this scenario, one would expect an excess of material at apocenter due to the slower orbital motion there. In order to see whether our data show such an effect, we have simulated the tau map using the results of dynamical modeling for a forced eccentricity of 0.06, and the result is shown in the right hand panel of Figure 3. Although the model tau map shows two equal peaks (in agreement with the estimated tau map), the NNW ansa (apocenter) is more radially extended than the SSW ansa since the orbits of individual grains are more dispersed there, and hence the integrated column density at apocenter is greater. A comparison of integrated column density in the two halves of the ring (apocenter and pericenter), as inferred from the model and estimated tau maps (truncated at a dust temperature of 35 K), indicates a predicted 12% apocentric excess from the model, as compared to a value of  $(14 \pm 3)\%$  estimated from the observations. The agreement between these values supports the interpretation in terms of forced eccentricity.

If the orbit of the perturbing body (presumably a planet) is within the inner boundary of the ring, our models indicate that a forced eccentricity of 0.06 would require an orbital eccentricity of  $\epsilon \simeq 6/a_{[\text{AU}]}$  for the planet, over a wide range of the planet’s semi-major axis,  $a$ . For example, if the inner edge of the ring is associated with the planet’s 2:3 mean motion resonance (analogous to Neptune and the Kuiper Belt in our own Solar System), then  $a \sim 86$  AU and  $\epsilon \sim 0.07$ . A constraint on the planet’s mass can be derived from the timescale required to produce the observed perturbation; the estimated age of Fomalhaut ( $\sim 200$  Myr) then implies a value of  $> 1$  Earth mass.

An additional asymmetry is apparent in the estimated tau map of Figure 3, in that the ring has a slight “teardrop” shape, being more pointed at pericenter. This effect is apparent in the  $350 \mu\text{m}$  data alone (see Figure 1) and also in a tau map made independently using only the 24, 70, &  $160 \mu\text{m}$  *Spitzer* images (not reproduced here). A possible explanation is warping of the disk, whereby the SSE portion of the ring has greater inclination to the line of sight than the NNW portion. To maintain such a warp would require at least two planets, since perturbations by a single planet would result simply in the disk adjusting to that planet’s orbital plane.

Stronger constraints on the properties of the orbiting body (or bodies) could be obtained from a more detailed knowledge of the azimuthal structure of column density around the ring, which would require a more accurate pole-on view than we were able to obtain with these data. Such information could, in principle, be obtained by supplementing the present data using additional observations including, for example, the SED mode of MIPS, and

submillimeter mapping at higher signal to noise ratio.

We thank Dr. Matt Bradford for his assistance during the observations. This work was performed by the Jet Propulsion Laboratory, California Institute of Technology, under contract with the National Aeronautics and Space Administration. Research at the Caltech Submillimeter Observatory is supported by NSF grant AST-0229008.



## REFERENCES

- Aumann, H. H., Fowler, J. W. & Melnyk, M. 1990, *AJ*, 99, 1674
- Backman, D. E. & Paresce, F. 1993, in *Protostars and Planets III* (Tucson: Univ. Arizona Press), 1253
- Backus, C., Velusamy, T., Thompson, T.J., Arballo, J., 2005, in *ADASS XIV*, Eds. P.L. Shopbell, M.C. Britton, & R. Ebert, *APS Conf. Ser.* (in press)
- Chini, R., Krügel & Kreysa, E. 1990, *A&A*, 227, L5
- Dent, W. R. F., Walker, H. J., Holland, W. S., & Greaves, J. S. 2000, *MNRAS*, 314, 702
- Dowell, C. D., et al. 2003, in “Millimeter and Submillimeter Detectors for Astronomy”, ed. T. G. Phillips & J. Zmuidzinas, *Proc. SPIE*, 4855, 73
- Holland, W. S. et al. 2003, *ApJ*, 582, 1141
- Lucy, L. B. 1974, *AJ*, 79, 745
- Quillen, A. C. & Thorndike, S. 2002, *ApJ*, 578, L149
- Richardson, W. H. 1972, *J. Opt. Soc. Am.*, 62, 55
- Rieke, G. H. et al. 2004, *ApJS*, 154, 25
- Stapelfeldt, K. R. et al. 2004, *ApJS*, 154, 458
- Werner, M. W. et al. 2004, *ApJS*, 154, 1
- Wilner, D. J., Holman, M. J., Kuchner, M. J. & Ho, P. T. P. 2002, *ApJ*, 569, L115
- Wyatt, M. C. et al. 1999, *ApJ*, 527, 918

Table 1. Results of parameter fit.

Parameter	Estimated value	Comment
$i$	$68^\circ \pm 1^\circ$	Inclination with respect to the plane of the sky
$\theta$	$-23^\circ \pm 1^\circ$	Position angle of tilt axis
$r_{\text{in}}$	$113.0 \pm 0.3$ AU	Inner radius
$r_{\text{out}}$	$238 \pm 1$ AU	Outer radius
$\psi_{100}$	$17^\circ \pm 1^\circ$	Opening angle for the flared-disk geometry
$\gamma$	$0.10 \pm 0.05$	Power-law index for radial variation of $\psi$
$\tau(r_{\text{in}})$	$(1.6 \pm 0.1) \times 10^{-3}$	Optical depth (normal to disk plane) at $r = r_{\text{in}}$ ; $\lambda = 24 \mu\text{m}$
$\alpha$	$1.73 \pm 0.01$	Power-law index for radial variation of column density
$\beta$	$1.02 \pm 0.01$	Power-law index for wavelength variation of opacity
$\Delta x, \Delta y$	$0.4 \pm 0.4; 7.6 \pm 0.4$	Offsets of dust ring from star in AU (see text)

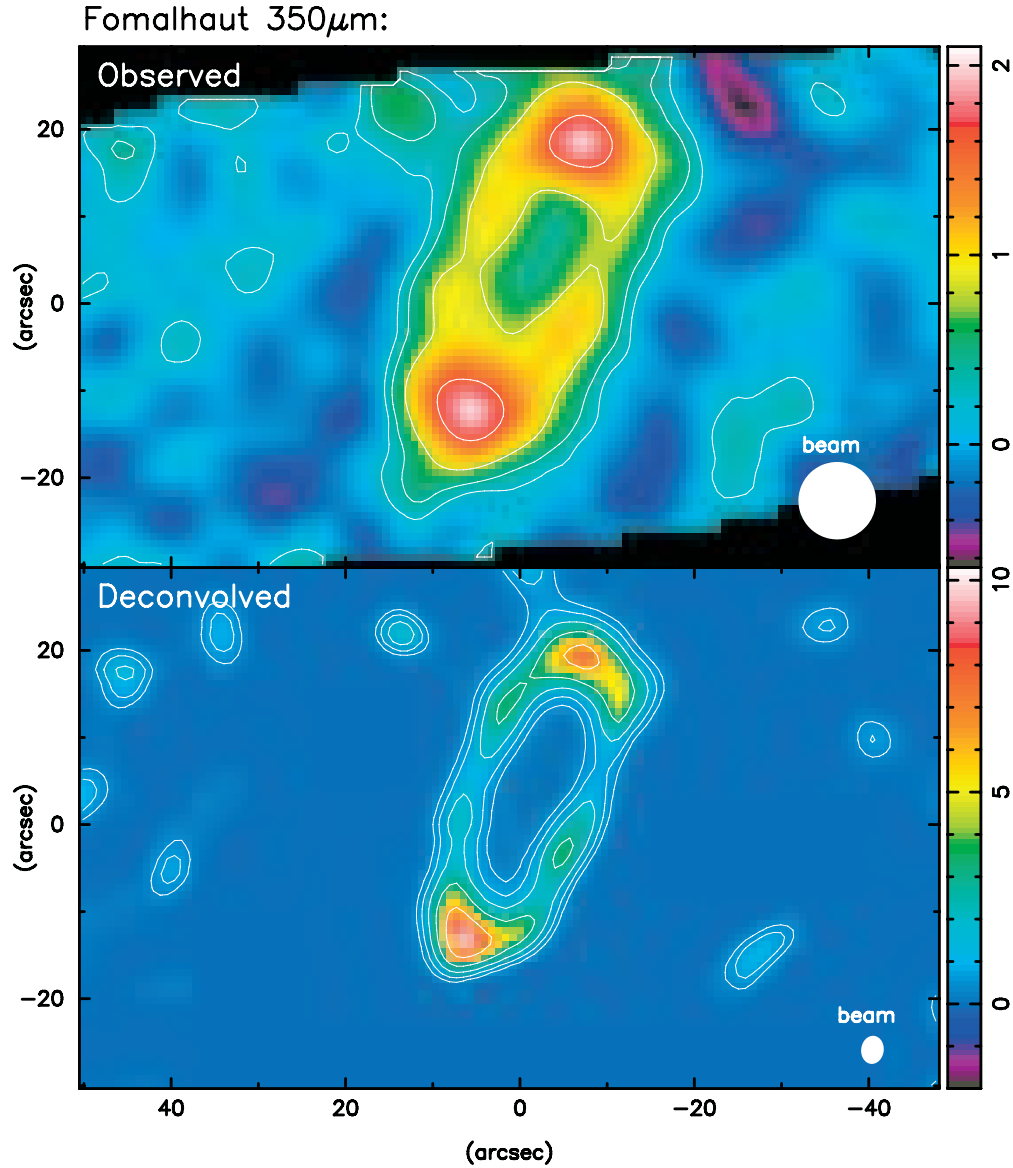


Fig. 1.— Fomalhaut at 350  $\mu\text{m}$ . The upper and lower panels represent the observed and deconvolved images, respectively. In the observed image the contours are at 0.2, 0.4, 0.8, & 1.6 mJy arcsec<sup>-2</sup> and the RMS noise is 0.15 mJy arcsec<sup>-2</sup>. In the deconvolved image the contours are at 0.4, 0.8, 1.6, 3.2, & 6.4 mJy arcsec<sup>-2</sup> and the RMS noise is 0.18 mJy arcsec<sup>-2</sup>.

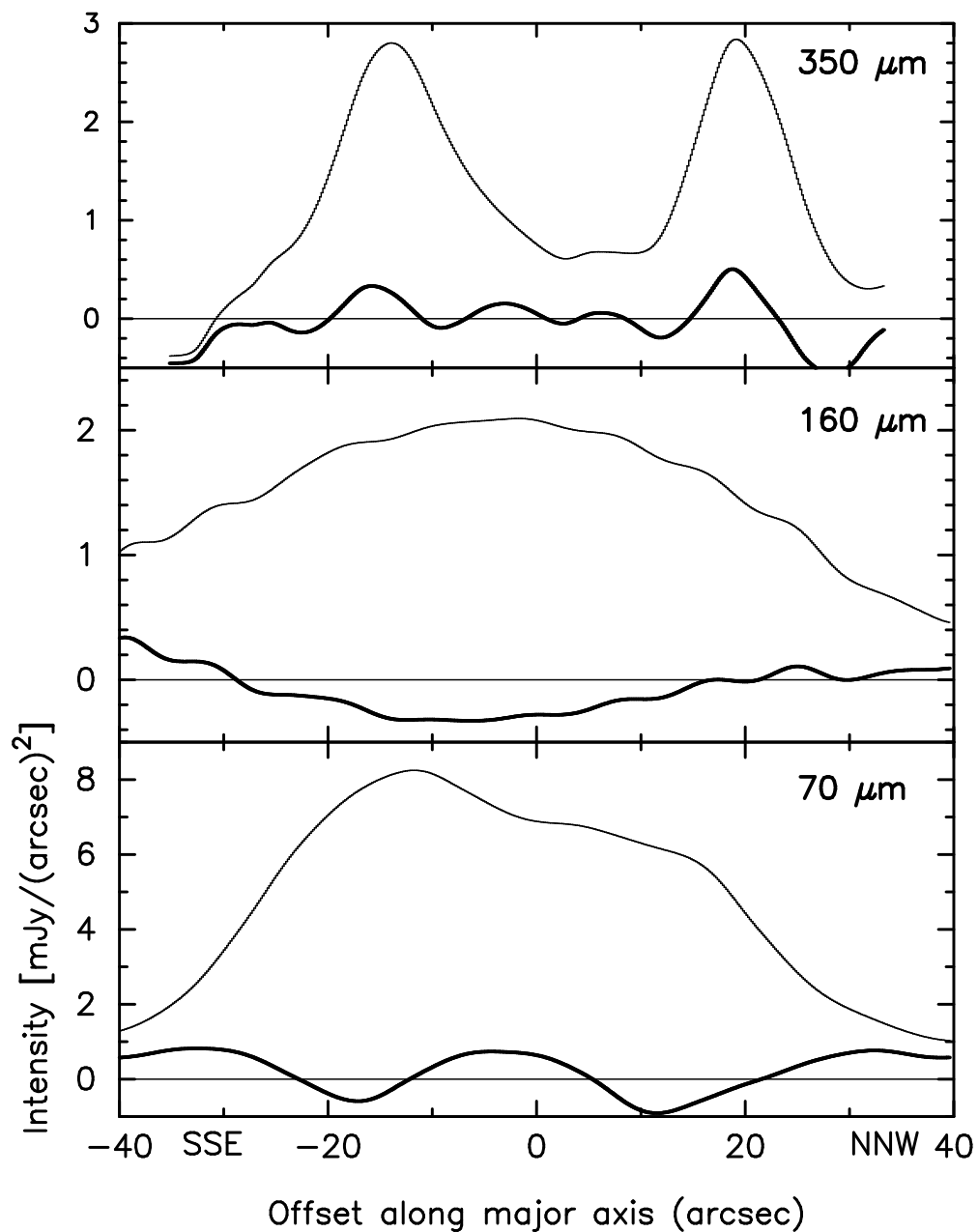


Fig. 2.— The residuals of the uniform-ring model at 350, 160, and 70  $\mu\text{m}$  (shown by the thick lines), as compared to the observed images (thin lines). The plots represent a slice through the images along the major axis of the tilted ring. The corresponding PSF widths (FWHM) were 9", 35", and 16" at 350, 160, and 70  $\mu\text{m}$ , respectively, and the absolute positional uncertainties were 2", 3", and 3", respectively.

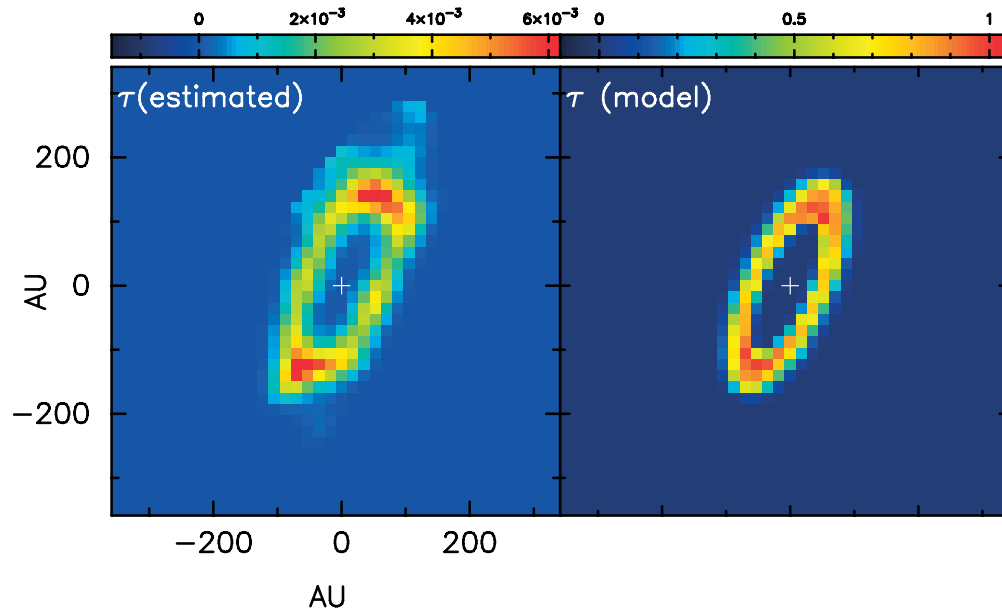


Fig. 3.— Estimated and model tau maps of Fomalhaut, projected onto the plane of the sky. *Left:* Estimated tau map, expressed at a reference wavelength of  $24 \mu\text{m}$ ; the peak line-of-sight optical depth is  $(6.61 \pm 0.26) \times 10^{-3}$ , with the uncertainty increasing by a factor of 2 at the low intensity edges of the ring. *Right:* Theoretical tau map in relative units, obtained using a dynamical model based on a forced eccentricity of 0.06. This model map has not been smoothed with an instrumental response, and therefore has a sharper appearance than the estimated tau map at the left.